14th International Symposium on Turbulence and Shear Flow Phenomena (TSFP14)
Heidelberg, Germany, July 28-31, 2026

EFFECTS OF FLOW CONTROL ON DRAG AND WAKE DYNAMICS OF A VEHICLE MODEL

Mohammed Khalid Hossen
Department of Mechanical Engineering
Dalhousie University Halifax, NS, Canada
khalidhossen@dal.ca

Mohammad Saeedi
Department of Mechanical Engineering
Dalhousie University Halifax, NS, Canada
Mohammad.saeedi@dal.ca

ABSTRACT

This study investigates the effectiveness of unsteady suction actuation applied near the upper edge of the slant surface of a 25° Ahmed body at a Reynolds number of 7.6×10^5. After the validated baseline case, unsteady suction applied at the optimum momentum coefficient yields an approximately 12% reduction in drag. The analysis demonstrates that this improvement is directly associated with changes in the separation bubble, shear-layer development, and overall wake structure. These flow modifications are illustrated using mean velocity, pressure coefficient, and Q-criterion contours, and are further supported by quantitative turbulence statistics. Unsteady actuation achieves a 12% drag reduction by increasing the base pressure and reducing the pressure drag, while shrinking the recirculation zone by 28% and modifying C-pillar vortices and quadrupole structures.

Keywords- Large-eddy simulation; active flow control; drag reduction; wake dynamics; vehicle model.

INTRODUCTION

Aerodynamic drag plays a critical role in vehicle fuel consumption. In response, the automotive industry is pursuing ambitious targets to reduce aerodynamic drag without compromising vehicle design or function [1]. For most road vehicles, the primary source of this drag is flow separation at the rear, where the bluff body geometry creates a highly unsteady, three-dimensional wake. This wake contains coherent structures, including transverse and C-pillar vortices, which are major contributors to pressure drag and thus present key opportunities for flow control [2].

Among Ahmed body configurations, the 25° slant angle has gained importance in both fundamental and applied research [3, 4]. At this slant angle the flow separates at the leading edge, forms a separation bubble, and reattaches before reaching the trailing edge, creating complex structures that strongly affect drag [5]. The wake contains transverse vortices from the slant edge, longitudinal so-called C-pillar vortices along the slant sides, and a recirculation region behind the vertical base [1]. These features are sensitive to boundary conditions, making the 25° configuration a challenging case for assessing flow control strategies [4, 2]. Active flow control (APC) has therefore gained interest as a more flexible alternative, offering on-demand operation to unsteady wake dynamics [6].

One promising class of AFC is synthetic jets, which operate on a zero-net-mass-flux principle by alternately ingesting and expelling fluid through an orifice [1, 6]. Synthetic jets have demonstrated significant potential for drag reduction in both experimental and numerical studies of the bluff body flows. For instance, Bai et al. [7] studied active flow control of a square cylinder wake using a synthetic jet applied at one leading edge based on the strong coupling between separating shear layers and near-wake dynamics. Large-eddy simulations (LES) demonstrated that the effectiveness of the synthetic jet depends on both the actuation frequency and momentum coefficient. Significant reductions in time-mean drag and fluctuating lift were achieved at high actuation frequencies and momentum coefficients of approximately 39% and 33%, respectively. In their study, synthetic jets substantially modify the near-wake flow structures.

Zhang et al. [8] experimentally investigated drag reduction of a 25° Ahmed body using steady blowing actuation applied around the rear-window and base edges. Individual actuations achieved drag reductions of 6-14%, while the combined actuation strategy produced a substantial drag reduction of approximately 29%. Their study showed significant wake modifications, including reduced separation bubbles and weakened C-pillar vortices. Zhang et al. [6] investigated the application of zero-mass active flow control for aerodynamic drag reduction on a 25° Ahmed body using LES and wind tunnel experiments. Their control strategy significantly reduced drag for a single vehicle and improved aerodynamic performance in a two-vehicle platoon. The actuation stabilized the wake flow, reduced unsteady fluctuations, and enhanced shear-layer dynamics.

In addition, other active flow control techniques, including steady or time dependent blowing and suction, have been widely investigated to clarify the underlying flow physics. For example, Wang et al. (2019) investigated near wake flow control behind a 25° Ahmed body using LES. An active unsteady jet derived from a synthetic jet was applied along the rear separation edges to reduce aerodynamic drag. The influence of jet actuation on wake topology and rear surface pressure was examined with particular attention to the forcing frequency. The results showed that appropriate actuation settings achieved drag reductions of up to 13.6% and were closely linked to changes in rear pressure distribution. Deng et al. (2024) experimentally investigated active drag reduction on an Ahmed body with a rear slant angle corresponding to the low drag regime using both single and combined steady blowing actuations [15]. Their results demonstrated that independently deployed jets around the rear slant and base edges produce measurable drag reduction, while an artificial intelligence-based control strategy identifies near optimal combinations of actuations. By accounting for both drag reduction and actuation power in the cost function, their study showed that substantial drag reduction can be achieved.

Previous numerical studies on active flow control of the 25° Ahmed body have investigated different momentum coefficients and actuation slot locations to reduce drag with different techniques. However, the effectiveness of unsteady suction control at relatively high Reynolds numbers has not been studied in terms of identifying an optimal actuation force coefficient. This study aims at addressing this gap by conducting a high-fidelity wall-resolved LES of an unsteady suction on a 25° Ahmed body. The goal of this work lies in establishing a clear connection between targeted momentum injection and drag reduction through an examination of changes in the separation bubble, shear layers, and wake topology. The remainder of this paper is structured as follows.

BOUNDARY CONDITIONS AND GOVERNING EQUATIONS

Figure 1 presents an overview of the computational and geometric configuration used to simulate the flow. The geometry of the Ahmed body is detailed in figure 1a, including its characteristic dimensions (length $L = 1.044\ m$, width $W = 0.389\ m$, and height $H = 0.288\ m$) and the 25° slant angle, a configuration widely used as a benchmark [3]. Figure 1b shows the computational domain, extending $52H$, $20H$, and $20H$ in the streamwise, wall-normal, and spanwise directions, respectively, with H being the model height and a uniform free-stream velocity of $U_\infty = 40\ m/s$. Simulations are performed at Reynolds number of $Re_H = U_\infty H/\nu = 7.6 \times 10^5$. The Ahmed body is positioned symmetrically within the computational domain, with its leading edge located $18H$ downstream from the inlet boundary.

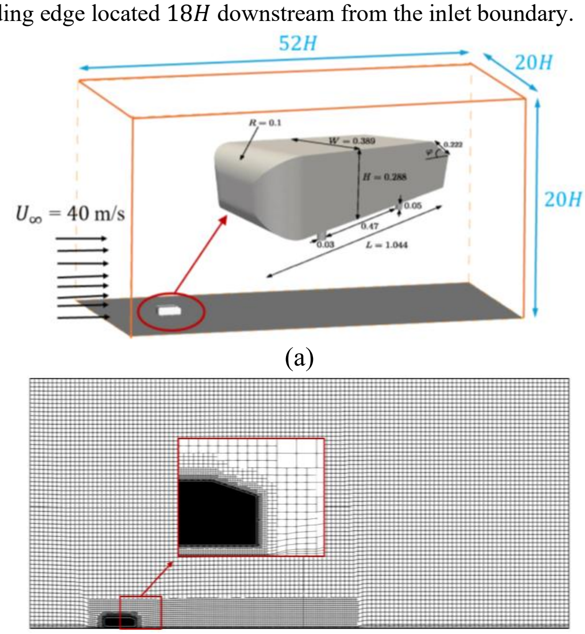

(b)

Figure 1. (a) Schematic representation of the computational domain. (b) Two-dimensional surface mesh refinement in the *x-y* plane ($Z/H = 0$).

The discretization strategy employs the snappyHexMesh utility within the Open-source package field operation and manipulation (OpenFOAM) framework. The resulting mesh comprises approximately 20 million hexahedral cells. To resolve the high-gradient flow features of the body wake, a mesh-refinement region extending about four vehicle lengths downstream and two vehicle widths on each side in the spanwise direction is applied. A uniform velocity field $(u, v, w) = (U_\infty, 0, 0)$ is imposed at the inlet and a Neumann boundary condition is imposed to velocity and pressure at the outlet. Free-slip conditions are applied at the top boundary and lateral walls, whereas no-slip conditions are enforced on the ground plane and the Ahmed body surfaces. The wall-normal grid spacing is $y^+ = u_\tau \Delta y/\nu$, where u_τ denotes the friction velocity and Δy represents the first cell height. In the present mesh, $y^+ \approx\ 0.93$ on the Ahmed body surfaces and 0.67 on the ground surface. The near-wall grid resolution on the Ahmed body surface is characterized by a streamwise wall-unit spacing of approximately $\Delta x^+ \approx 92$, while the spanwise wall-unit spacing is estimated as $\Delta z^+ \approx 17$ based on the local near-wall mesh spacing. The mesh quality metrics indicate acceptable performance, with a maximum aspect ratio, maximum non-orthogonality, and maximum skewness. In addition, the boundary openness, cell openness, face area, cell volume, zero illegal faces and face pyramid checks were all satisfactory, confirming that the mesh quality is acceptable for the present simulations. The total number of cells is kept the same in both the uncontrolled and controlled simulations.

Large-eddy simulation of the incompressible flow is performed by solving the filtered continuity and momentum equations, while the wall-adaptive local eddy viscosity (WALE) model is used for subgrid-scale closure [10,11]. A second-order implicit backward scheme was applied for temporal discretization, while second-order central differencing schemes were used for both convective and diffusive spatial terms, which provide numerical stability and consistency [9]. The governing equations were solved using the Pressure Implicit with Splitting of Operators (PISO) algorithm. To maintain numerical stability and accurately resolve unsteady flow features, the simulations were advanced with a constant physical time step of $\Delta t\ =\ 1\ \times 10^{-6}$s. The temporal resolution was carefully chosen to keep the Courant–Friedrichs–Lewy (CFL) number below 0.4. Further, for a more accurate prediction of the flow, two corrector steps have been used. Flow statistics collected after the initial 10 flow-through times (FTTs) to ensure that the flow had reached a statistically stationary state after 2 FTTs. Overall, 384 cores were utilized to conduct parallel computation with 64k and 90k of CPU-hours spent for uncontrolled and controlled cases, respectively.

RESULT DISCUSSION

A. ASSESSMENT OF MESH RESOLUTION

The fidelity of LES strongly depends on the ability of the computational grid to adequately resolve the turbulent flow. Insufficient grid resolution increases reliance on the SGS model, which may lead to inaccurate predictions of the flow. To quantitatively evaluate the adequacy of grid resolution in the present study, we employ the resolution parameter $M = k_{sgs}/(K_{res} +\ k_{sgs})$, where k_{sgs} is the SGS turbulent kinetic energy defined as k_{sgs} =1/2(u'^2), and the term K_{res} represents the resolved turbulent kinetic energy, defined as K_{res} = $1/2\ (\bar{u}'^2 + \bar{v}'^2 + \bar{w}'^2)$[12]. This metric ranges from $M = 0$, ideally representing a direct numerical simulation where all turbulent scales are fully resolved, to $M = 1$, corresponding to a Reynolds-Averaged Navier-Stokes approach in which all turbulent energy is modeled. In the present study, the domain averaged mixing fraction is found to be $M = 0.0126$, as shown in figure 2 demonstrating the value of M across all computational cells. It indicates that on average, only 1.26% of the total turbulent kinetic energy is modeled, while the remaining 98.76% is directly resolved by the computational mesh. Such a low value of M demonstrates that the grid resolution is sufficiently fine to capture the dominant energy-containing eddies, because Pope [12] suggests that a reliable LES grid should resolve the 80% of the turbulent kinetic energy.

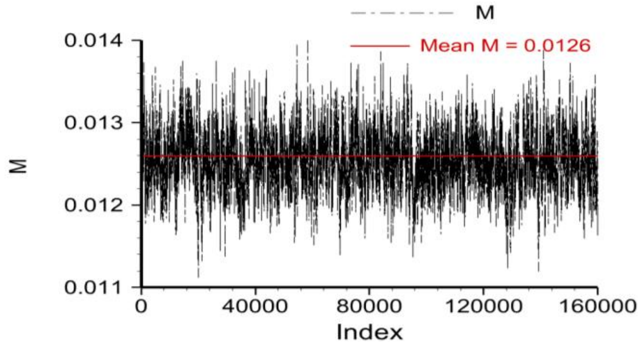

Figure 2. Evolution of the mixing factor M. The dashed black line represents instantaneous values of M, while the red solid line indicates the mean value.

B. VALIDATION

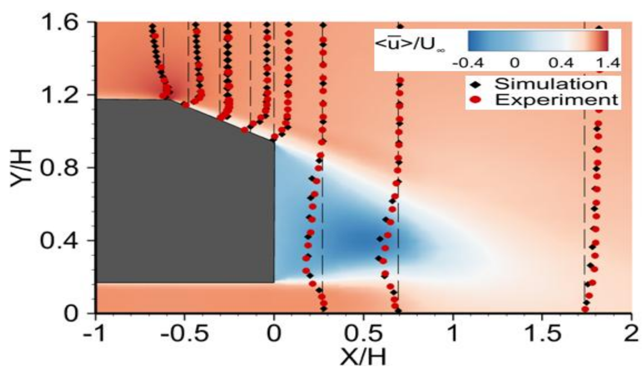

(a) Mean resolved velocity, $\langle \bar{u} \rangle / U_\infty$

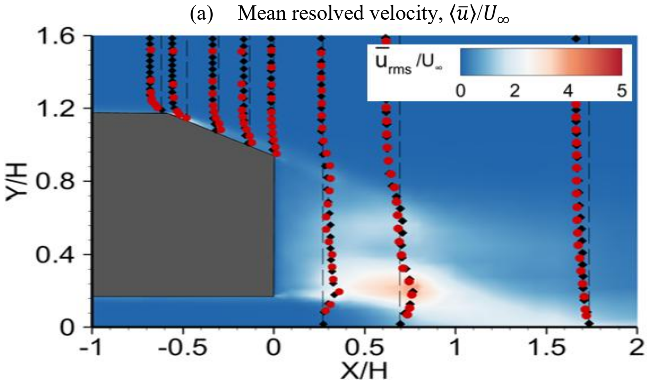

(b) Mean resolved streamwise stresses, $\bar{u}_{rms}/{U_\infty}^2$

Figure 3. Validation of the simulation (uncontrolled) against experimental data in the vertical x-y plane ($Z/H = 0$): (a) the mean resolved streamwise velocity and (b) the mean resolved streamwise normal stresses.

For the accuracy of the numerical approach, the LES results for the uncontrolled case are validated against the reference data reported in [3] and [13]. Figure 3 presents a quantitative comparison of the first- and second-order statistics in the vertical x-y plane. The vertical profiles of the mean streamwise resolved velocity in figure 3a show very good agreement between the simulation and the experimental data across all streamwise stations. The LES accurately reproduces the velocity field, as well as the position and shape of the separated shear layer that forms along the slant and farther downstream. Small differences appear within the recirculation zone, particularly near $X/H = 0.5$, where the simulation slightly underestimates the strength of the reverse flow. The typical relative difference between the LES and experimental results at this location is less than 1%. Apart from this reverse flow region, the agreement across the entire vertical profile is excellent. The comparison of the streamwise resolved Reynolds normal stress in the figure 3b provides further support for the fidelity of the simulation. The LES correctly predicts both the location and the intensity of the stress peak associated with the turbulent shear layer. A mild overprediction of the peak stress is observed at $X/H = 0.3$, while the peak stress at $X/H = 0.7$ is slightly underpredicted. Particularly, relative difference of LES and experiment in this location is less than 1%. Despite these differences, the overall match is very good, and the simulation captures the highest stresses and spatial distribution.

C. FLOW CONTROL STRATEGY

For the uncontrolled case, the time-averaged drag coefficient of 0.310 shows good agreement with 0.285 reported by Ahmed et al [3]. After establishing satisfactory agreement for the baseline case, the present study proceeds to investigate drag reduction using unsteady suction control through a continuous actuation slot located at the leading edge of the slant surface [2]. The slot has a spanwise width of $w = 0.283$ m, corresponding to approximately 98% of the body span W, and a slot thickness of $d = 1 \times 10^{-3}$ m. The wall-normal suction velocity is prescribed as $V_{\text{jet}} = -|\ 0.4\pi U_f \sin(2\pi f_s t)\ |$, where the negative sign denotes suction-dominated actuation, U_f and f_s are the actuation velocity and frequency, respectively. The streamwise and spanwise velocity components at the slot are set to zero, i.e. $U_{\text{jet}} = W_{\text{jet}} = 0$. The dominant excitation frequency is therefore $f_c = 2f_s$, which is defined as the control frequency. The actuation amplitude is characterized by the amplitude ratio $A^* = U_f/U_\infty = 0.8$. To identify an optimal control frequency, five actuation frequencies are considered, such as $f_c = 68$, 136, 272, 544, and 1088 Hz. The actuation strength is quantified using the momentum coefficient, $C_\mu = 2\, V_{\text{jet}}^2\, A_{\text{slot}}/U_\infty^2\, A_{\text{ref}}$, where $A_{\text{slot}} = wd$ is the actuation slot area, A_{ref} is the frontal reference area of the Ahmed body. Among the tested configurations, the case with $A^* = 0.8$ and $f_c = 544$Hz provides the most effective drag reduction. With suction actuation (controlled case), the drag coefficient decreases to C_d=0.274, corresponding to an overall drag reduction of approximately 12% relative to the uncontrolled case ($C_d = 0.310$).

D. Flow Topology

In figure 4a, the mean resolved velocity streamlines in the uncontrolled case indicate a wake dominated by two primary vortices [5]. The upper vortex (A) is centered at $X/H \approx 0.4, Y/H \approx 0.65$ and rotates clockwise, whereas the lower vortex (B) is located at approximately $X/H \approx 0.4, Y/H \approx 0.3$ and rotates counterclockwise. The point labeled M corresponds to a saddle point in the flow topology. This point governs wake organization as in real automotive wakes, where small shifts of the saddle point can enlarge or contract recirculation bubble, directly impacting drag and vehicle stability. The streamline meets the ground plane at a reattachment point located at $X/H \approx 3.6$. The position is associated with the low-pressure recirculation zone.

Figure 4b shows the controlled case that substantial changes in the streamwise resolved mean flow topology, which alters the wake characteristics. The upper vortex (C) is displaced downward and reduced in size, while the lower vortex (D) also decreases to extent relative to the uncontrolled case in figure 4a. The point labeled N represents saddle point and its position has shifted upstream compared to the uncontrolled case in figure 4a. This reorganization of the wake structure is consistent with recent findings showing that unsteady suction can manipulate the separating shear layers that define the recirculation regions [2]. The most notable change in the controlled case is the reduction in reattachment length, which decreases to approximate $X/H \approx 2.6$, corresponding to approximately 28% reduction relative to the uncontrolled case. The shortened wake is associated with reduced form drag and supports the mechanisms proposed for active wake flow control.

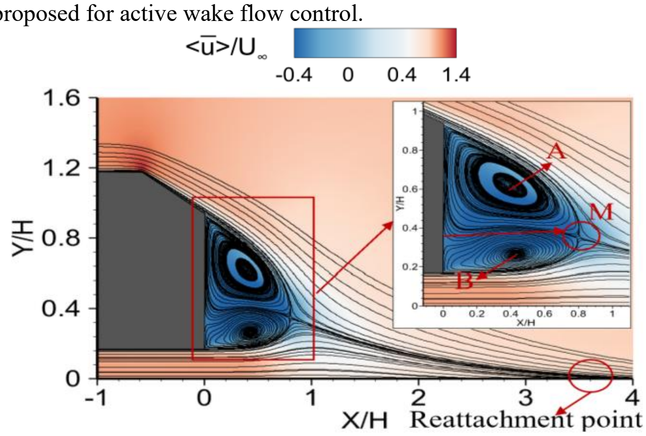

(a) Uncontrolled

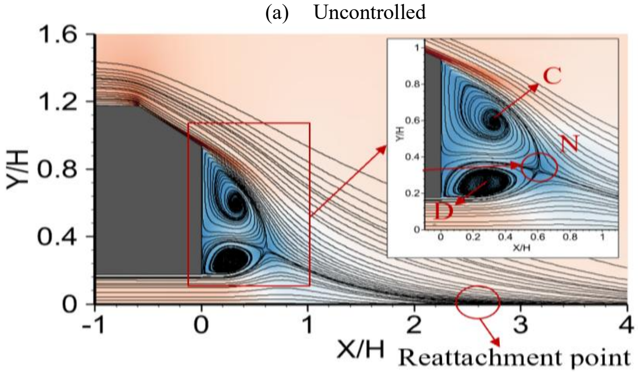

(b) Controlled

Figure 4. Time-averaged streamlines superimposed on the contours of streamwise resolved velocity $\langle \bar{u} \rangle / U_\infty$ in the *x*-*y* plane ($Z/H = 0$).

Figure 5a illustrates the resolved instantaneous vortical structures for the uncontrolled and controlled cases. These structures are visualized using second invariant of the velocity gradient tensor, known as the Q-criterion, and defined as $Q = 1/2(R_{ij}R_{ij} - S_{ij}S_{ij})$. It identifies regions where the magnitude of the rotation-rate tensor (R_{ij}) exceeds that of the strain-rate tensor (S_{ij}), thus highlighting the cores of coherent vortices [14]. In the uncontrolled case (figure 5a), the resolved instantaneous vortex field exhibits the characteristic features of the canonical Ahmed body wake. The flow separates sharply at the upper edge of the slant surface, producing a thick separation boundary layer that rolls up into complex interacting vortical structures. The large counter-rotating so-called C-pillar vortices that originate from the lateral shear layers at the slant edges. These structures are energetic, remain coherent and form a persistent dipole vortex system that regulates much of the far wake behaviour. In the recirculation zone, reverse bubbles reflecting the shear layer instability of the separated wake. Figure 5b presents the mean resolved velocity iso-surfaces of Q-criterion for both cases. For the uncontrolled case (top half of the symmetry line), the wake is governed by a set of large, highly coherent vortical structures [1]. The separation at the side edges of the slant generates two strong counter rotating C-pillar vortices that retain their coherence as they convect downstream. A recirculation bubble forms immediately behind the vertical base, marking the region of reverse flow bounded by a separation boundary layer. As the C-pillar vortices propagate farther downstream, they develop into a long and well-defined dipole vortex pair that persists over several body heights. These structures remain coherent far downstream in the upper portion of the wake, which in turn generates a quadrupole-like arrangement for the full body. In the controlled case (bottom half of the symmetry line), the application of the unsteady suction induces a fundamental reorganisation of the mean wake. The most notable effect is the strong suppression of the primary vortical features. The C-pillar vortices become significantly smaller, weaker and less coherent. The time-averaged recirculation bubble shrinks, indicating a reduction of the reverse flow region. The dipole vortices in the far wake are less organised and decay rapidly, demonstrating that the control weakens the large-scale motions.

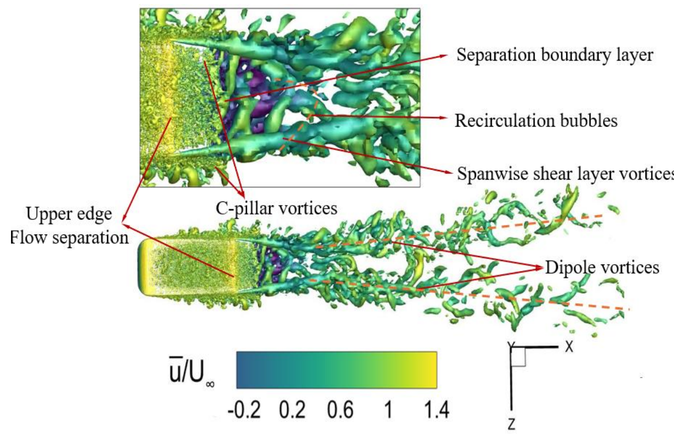

(a)

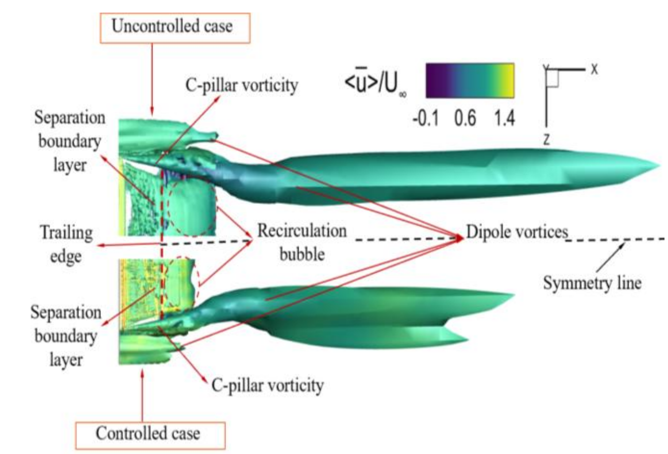

(b)

Figure 5. shows the corresponding mean resolved velocity structures representing the mean flow ($Q = 0.2$). The colors of mean resolved velocity fields are normalized by U_∞.

Figures 6a and 6b present iso-surfaces of the pressure coefficient defined as $C_p = (P - P_\infty)/q_\infty$ where P_∞ and $q_\infty = 1/2\rho U_\infty{}^2$ are the static and dynamic pressures, respectively, to capture the core of the low-pressure region in the uncontrolled and controlled cases. In the uncontrolled case (figure 6a), the C_p iso-surface encloses a compact volume downstream of the body, highlighting a distinct region of relatively low pressure. The coloring by mean resolved streamwise velocity ($\langle \bar{u} \rangle / U_\infty$) indicates that within this low-pressure region, the velocity is predominantly negative ($\langle \bar{u} \rangle$ / $U_\infty = -0.2$ to -0.6), highlighting the presence of a recirculation zone with reversed flow. This large region of reversed flow and low pressure constitutes a major contributor to the overall aerodynamic drag [1]. Upon activation of the control mechanism (figure 6b), the C_p iso-surface expands significantly in volume and shifts closer to the body. The coloring indicates a clear re-energization within this iso-surface, characterized by a shift toward less negative streamwise resolved mean velocities ($\langle\bar{u}\rangle/U_\infty = 0.2$ to 0.6). These results suggest that the control case mitigates the low-pressure region while enhancing the mean velocity inside the wake, as a result altered the recirculation zone.

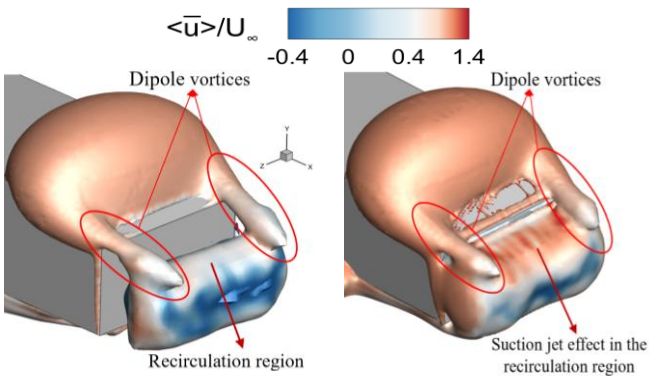

(a) Uncontrolled Controlled

Figure 6. Iso-surface pressure coefficient C_p (-0.14) colored by normalized mean resolved velocity.

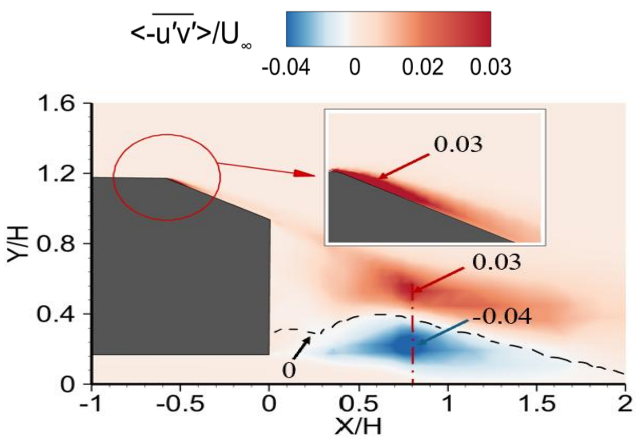

(a)

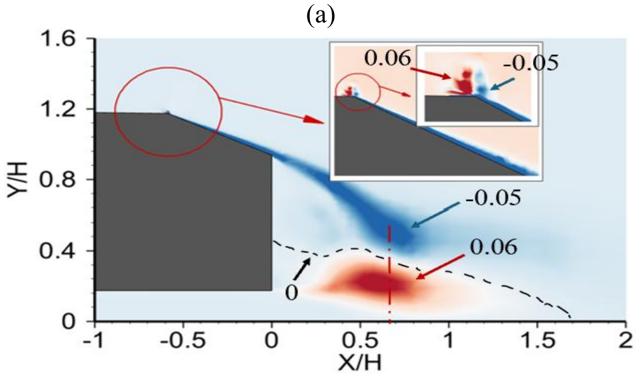

(b)

Figure 7. Spatial distribution of the shear components of the resolved Reynolds stress in the mid-vertical *x-y* plane ($Z/H = 0$).

Figure 7a shows the resolved Reynolds shear stress -$\langle\overline{u'v'}\rangle/U_\infty{}^2$ for the uncontrolled case. A positive peak of approximately 0.03 is observed after leading and trailing edge separation in the shear layer. In contrast, the lower recirculation region exhibits a negative peak of approximately -0.04. These peaks highlight the momentum deficit in the wake. In contrast, figure 6b shows that in the controlled case, the -$\langle\overline{u'v'}\rangle/U_\infty{}^2$ distribution is significantly altered, indicating a modification of turbulent momentum transport. In the upper shear layer, the positive peak is double about 0.06 at ($X/H, Y/H \approx 0.6, 0.2$). However, the negative peak in the main wake decreases nearly to -0.01 at ($X/H, Y/H \approx 0.6$, 0.2). The inset reveals a negative peak of -0.05 near the upper separation point, representing a substantial decrease in stress relative to the uncontrolled case in this region. The lower recirculation region exhibits a positive peak of approximately 0.06. Overall, the resolved Reynolds stresses in the controlled case are downstream of the leading-edge separation and within the reverse flow region, due to re-energization of the boundary layer by the suction actuation.

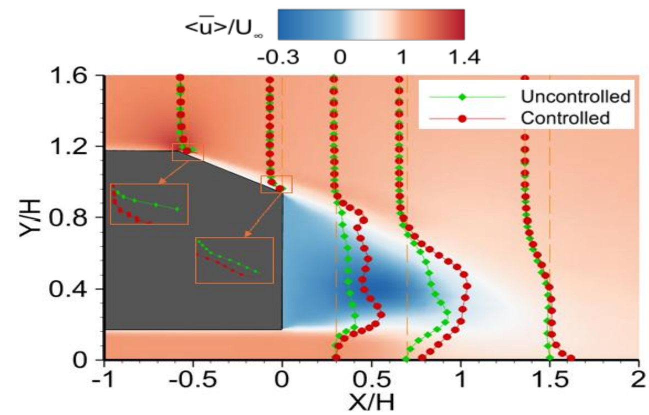

(a) TKE production

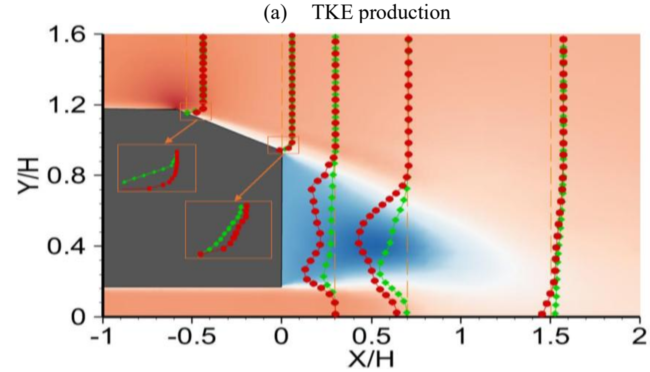

(b) Viscous dissipation

Figure 8. Vertical profiles of (a) TKE production and (b) viscous dissipation, overlaid on background contours of the mean resolved velocity and normalized by U_∞^3/H.

Figure 8a shows the vertical profiles of the TKE production at the selected streamwise locations, as discussed the TKE budget equation by Saeedi et al. [14]. The controlled case exhibits lower TKE production near the upper shear layer along the slant surface compared with the uncontrolled case at $-0.5 < X/H < 0$. At the streamwise locations $X/H = 0.3$ and $X/H = 0.7$, the TKE production is higher in regions where the turbulent flow separates from the vertical base edge. In these regions, the shear layers surrounding the recirculation zone exhibit higher TKE production for the controlled case than for the uncontrolled case, suggesting that suction control modifies the shear-layer dynamics in the separated flow. At the far-wake location $X/H = 1.5$, TKE production decreases for both cases. However, the uncontrolled case maintains slightly higher production levels. This behavior indicates that suction actuation generates strong local fluctuations after separation from the rear vertical base and enhances mixing along the surrounding separated shear layer. Figure 8b presents the vertical profiles of the normalized viscous dissipation at the same streamwise locations. This term represents the rate at which turbulent kinetic energy is converted into internal energy by viscous effects at the smallest scales. The controlled case exhibits dissipation levels that are approximately similar to uncontrolled case at $-0.5 < X/H < 0$. Further downstream at $0.3 < X/H < 0.7$, the controlled case shows a lower dissipation profile in the reverse flow region compared with the uncontrolled case, indicating reduced small-scale dissipation relative to the uncontrolled case. This behavior is consistent with the corresponding trends observed in the TKE production profiles at these locations. At the far-wake location $X/H = 1.5$, dissipation decreases for both cases; however, the controlled case shows dissipation levels slightly lower near the bottom wall than the uncontrolled case.

In figure 9a, the uncontrolled case exhibits streamwise higher PSD levels over the low- to intermediate-Strouhal number range ($0.01 < St < 1$), with a clear dominant peak around $St \approx 0.2$. The controlled case shows a reduction in PSD magnitude across this frequency range, including a lower amplitude at the dominant peak. At higher Strouhal numbers, both spectra decay slowly. In figure 9b, both uncontrolled and controlled cases exhibit a clear dominant peak of vertical PSD at approximately $St \approx 1.7$. The uncontrolled case shows higher PSD levels over the low-frequency range. The controlled case exhibits a reduced PSD magnitude across this range, while the peak location remains nearly same. It indicates that the effect of suction modify the shear layer near the actuation slot. While the inertial subrange shows energy transfer across frequencies and follows a slope of -5/3 [14].

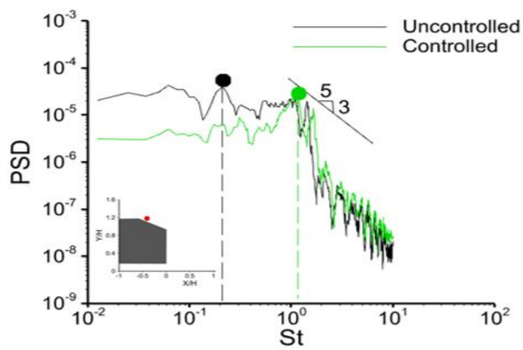

(a) Streamwise

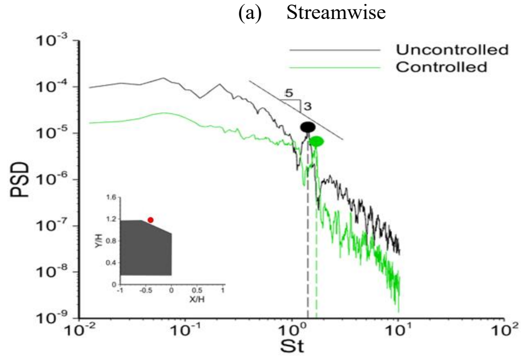

(b) Vertical

Figure 9. Power spectral density (PSD) of the (a) streamwise and (b) vertical resolved velocity fluctuation for the uncontrolled and controlled flow cases, evaluated at red location as shown in the inset.

CONCLUSIONS

This study investigates the effectiveness of unsteady suction jet actuation using wall resolved large eddy simulation. It provides insight into the control mechanisms responsible for wake flow modification through targeted boundary layer suction. In the present configuration, unsteady suction applied near the upper edge of the slant surface, with a momentum coefficient of 2.9×10^{-3}, produces a drag reduction of about 12%. Under controlled conditions, the classical two vortex recirculation pattern observed in the uncontrolled wake is clearly reorganized. The reattachment point moves upstream by about 28%, while the core of the reverse flow region shifts significantly upstream and downward. The mean Q-criterion analysis further confirms a substantial suppression of the wake separation legs. In addition, the spectral analysis shows that the control weakens and disrupts vortex shedding immediately downstream of the actuation slot, while also reducing the dominant low frequency peaks associated with large scale vortex shedding.

ACKNOWLEDGEMENT

The research fundings provided to Mohammad Saeedi from NSERC and Net Zero Atlantic are greatly acknowledged. The authors would like to acknowledge the Digital Research Alliance of Canada.

REFERENCES

[1] Zhang, B. F., Fan, D. W., & Zhou, Y., "Artificial intelligence control of a low-drag Ahmed body using distributed jet arrays," Journal of Fluid Mechanics, 963, A3 (2023).

[2] Wang, B. X., Yang, Z. G., & Zhu, H., "Active flow control on the 25 Ahmed body using a new unsteady jet," International Journal of Heat and Fluid Flow, 79, 108459 (2019).

[3] Ahmed, S. R., Ramm, G., & Faltin G. "Some salient features of the time-averaged ground vehicle wake," SAE transactions, 473-503 (1984).

[4] Kourta, A., & Leclerc, C., "Characterization of synthetic jet actuation with application to Ahmed body wake," Sensors and Actuators A: Physical, 192, 13-26 (2013).

[5] Serre, E., Minguez, M., Pasquetti, R., Guilmineau, E., Deng, G. B., Kornhaas, M., Schäfer, M., Fröhlich, J., Hinterberger, C., & Rodi, W., "On simulating the turbulent flow around the Ahmed body: A French-German collaborative evaluation of LES and DES," Computers & Fluids, 78, 10-23 (2013).

[6] Zhang, G., Song, X., Hu, X., Wang, J., Yu, T., Guo, P., & Li, J., "A review on the drag reduction of Ahmed body," Proceedings of the Institution of Mechanical Engineers, Part D: Journal of Automobile Engineering, 09544070241307072 (2025).

[7] Bai, H., Wang, F., Zhang, S., Zhang, W., & Lin, Y., "Square cylinder flow controlled by a synthetic jet at one leading edge," Physics of Fluids, 35(3) (2024).

[8] Zhang, B. F., Liu, K., Zhou, Y., To, S., & Tu, J. Y., "Active drag reduction of a high-drag Ahmed body based on steady blowing," Journal of Fluid Mechanics, 856, 351-396 (2018).

[9] Hossen, M. K., Asgari, E., Saeedi, M., & Nyantekyi-Kwakye, B., "Flow characteristics of three-dimensional offset jet over surface-mounted ribs using large-eddy simulation," Physics of Fluids, 37(5) (2025).

[10] Nicoud, F., & Ducros, F., "Subgrid-scale stress modelling based on the square of the velocity gradient tensor," Flow, turbulence and Combustion, 62(3), 183-200 (1999).

[11] Hossen, M. K., Mulayath Variyath, A., & Alam, J. M., "Statistical analysis of dynamic subgrid modeling approaches in large eddy simulation," Aerospace, 8(12), 375 (2021).

[12] Pope, S. B., "Ten questions concerning the large-eddy simulation of turbulent flows," New journal of Physics, 6(1), 35 (2004).

[13] Lienhart, H., & Becker, S., "Flow and turbulence structure in the wake of a simplified car model," SAE transactions, 785-796 (2003).

[14] Saeedi, M., Nyantekyi-Kwakye, B., and Asgari, E., "Energy and frequency analysisin the wake of a heavy-duty truck model using large-eddy simulation," J. WindEng. Ind. Aerodyn. 253, 105854 (2024).

[15] Deng, G., Fan, D., Zhang, B., & Zhou, Y., "Active control for a low-drag Ahmed vehicle model based on steady blowing," Physics of Fluids, 36(1) (2024).